Chinese Chemical Letters 33 (2022) 3212–3216

Contents lists available at ScienceDirect

Chinese Chemical Letters

journal homepage: www.elsevier.com/locate/cclet

Bi_2S_3 nanorods encapsulated in iodine-doped graphene frameworks with enhanced potassium storage properties

Yi Wei[a], Wenhui Hou[a], Peng Zhang[a,b], Razium A. Soomro[a], Bin Xu[a,*]

[a] State Key Laboratory of Organic-Inorganic Composites, Beijing Key Laboratory of Electrochemical Process and Technology for Materials, College of Materials Science and Engineering, Beijing University of Chemical Technology, Beijing 100029, China
[b] Beijing Advanced Innovation Center for Soft Matter Science and Engineering, Beijing University of Chemical Technology, Beijing 100029, China

ARTICLE INFO

Article history:
Received 29 August 2021
Revised 27 September 2021
Accepted 15 October 2021
Available online 21 October 2021

Keywords:
Bi_2S_3
Iodine-doped graphene
Potassium-ion battery
Anode materials
Nanorods

ABSTRACT

Bismuth sulfide (Bi_2S_3) is a promising anode material for high-performance potassium ion batteries due to its high theoretical capacity. However, the poor conductivity and substantial volume expansion hinder its practical application. We proposed an iodine-doped graphene encapsulated Bi_2S_3 nanorods composite (Bi_2S_3/IG) as an efficient anode for PIBs. The uniform-sized Bi_2S_3 nanorods evenly *in-situ* encapsulated in iodine-doped graphene framework, facilitating the electron transportation and structural stability. The potassium storage performance was evaluated in three electrolytes, with the best option of 5 mol/L KFSI in DME. The reversible capacity of representative Bi_2S_3/IG reached 453.5 mAh/g at 50 mA/g. Meanwhile, it could deliver an initial reversible capacity of 413.6 mAh/g at 100 mA/g, which maintained 256.9 mAh/g after 200 cycles. The proposed strategy contributes to improving potassium storage performance of metal sulfide anodes.

Potassium-ion batteries (PIBs) are regarded as a promising substitution of lithium-ion batteries (LIBs) based on their low cost, high ionic conductivity and the close redox potential of K^+/K (−2.93 V *vs.* SHE) to that of Li^+/Li (−3.04 V *vs.* SHE) [1–4]. However, the anode suffers from extensive volume expansion during potassiation process due to the large size of K ion (1.38 Å). For example, the volume expansion of graphite could reach as high as 61% when used as the anode of PIBs [5,6]. Moreover, the large size of K^+ results in slow charge kinetics and leads to inferior rate capability of the batteries. Thus, selecting and designing appropriate anode materials is crucial in the case of PIBs. In this regard, a variety of nanomaterials such as carbon materials [7–9], alloys [10,11], metal oxides [12,13] and metal sulfides (MSs) [14,15] have been explored as anode materials for PIBs.

Unlike carbon-based materials, which follow an intercalation mechanism, MSs rely on multiple processes including conversion and alloying reaction for potassium storage and form a cumulative mechanism with a large theoretical capacity [15]. Recently, some MSs, such as WS_2 [16,17], MoS_2 [18–20], CoS_2 [21], FeS_2 [22–24], CuS [25,26], Sb_2S_3 [27,28] and ZnS [29], have proven to be efficient in achieving high capacity, however, their poor electron conductivity and sluggish ion-diffusion rates usually lead to delayed reaction kinetics. In addition, the drastic volume change during potassiation/de-potassiation may result in the collapse of the electrode structure and impair the cycling performance. Controlling the morphology or constructing nanocomposites is a viable route to improve the performance of MSs-based anodes. For example, Peng *et al.* prepared a nitrogen-doped carbon coated Cu_2S hollow nanocube structure as anode of PIBs, realizing enhanced conductivity as well as efficient volume expansion mitigation [30]. Similarly, Li *et al.* designed Fe_7S_8/C hybrid nanocages reinforced by defect-rich MoS_2 nanosheets [31], which exhibited an enhanced structure stability with rapid K^+ diffusion rates. Bi_2S_3 is a layered semiconductor material widely utilized in photoelectric components and thermoelectric equipment, and also shows great potential for PIBs [32–34]. Besides conversion and alloying reaction, the unique layered structure enables the Bi_2S_3 with extra intercalation process for K^+ storage, resulting in higher potassium storage capacity. Moreover, its growth has a 1D preferred orientation trend and is easy to form nanowires or nanorods, which is beneficial for alleviating the large volume change during potassiation/de-potassiation process [35,36].

Herein, we reported an iodine-doped graphene encapsulated Bi_2S_3 nanorods composite (denoted as Bi_2S_3/IG) as the effective anode for PIBs. In the composite, the uniform sized Bi_2S_3 nanorods evenly encapsulated in the iodine-doped graphene framework. This unique structure design cannot only improve the conductivity of

* Corresponding author.
E-mail address: xubin@mail.buct.edu.cn (B. Xu).

https://doi.org/10.1016/j.cclet.2021.10.035
1001-8417/

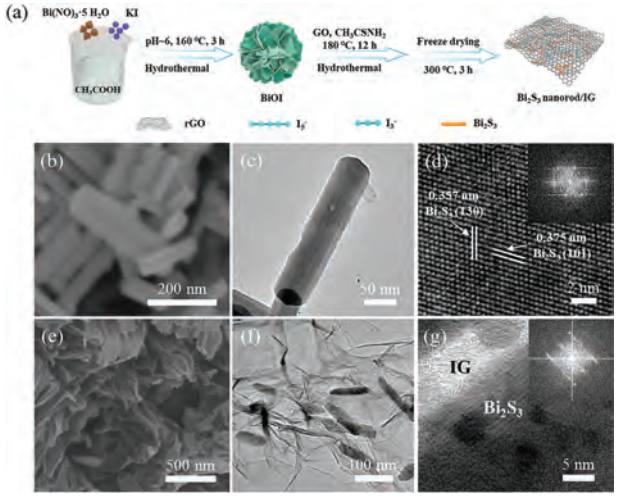

Fig. 1. Synthesis process and characterizations of the electrode materials. (a) Schematic diagram representing the synthesis of Bi_2S_3/IG. (b) SEM, (c) TEM and (d) HRTEM images (Inset: SAED pattern) of the Bi_2S_3 nanorods. (e) SEM, (f) TEM and (g) HRTEM images (Inset: SAED pattern) of the Bi_2S_3/IG composite.

the composites, but also alleviate the large volume expansion and maintain the structure stability during potassiation. These advantages endow the Bi_2S_3/IG nanocomposites with enhanced capacity, rate capability, and cycle stability as PIBs anode in reference to its pristine Bi_2S_3 counterpart. In addition, since electrolyte has a great influence on the potassium storage performance, three electrolytes (*i.e.*, 1 mol/L KFSI in EC/DEC, 1 mol/L KFSI in DME, and 5 mol/L KFSI in DME) were selected for optimum the potassium storage performance of the Bi_2S_3/IG electrodes. Among all, the Bi_2S_3/IG showed the best comprehensive performance with 5 mol/L KFSI in DME electrolyte in terms of capacity, cycle performance, and rate capability.

Fig. 1a showed the schematic illustration of the synthesis procedure for the Bi_2S_3/IG composite. BiOI nanoflowers were firstly synthesized through a hydrothermal process at 160 °C using $Bi(NO_3)\cdot 5H_2O$ and KI as precursors. The BiOI was then re-dispersed into graphene oxide dispersion and sulfurized with thioacetamide by hydrothermal method at 180 °C for 12 h In this process, Bi_2S_3 was *in-situ* grew and encapsulated in graphene framework, and iodine atoms decomposed by BiOI were captured by graphene to form iodine-doped graphene. Finally, after an annealing process under Ar atmosphere at 300 °C, the Bi_2S_3/I doped-rGO (denoted as Bi_2S_3/IG) was obtained. The morphologies of the materials were characterized using scanning electron microscopy (SEM) and transmission electron microscopy (TEM). The BiOI intermediates exhibited a nanoflower-like structure composed of multiple nanosheets (Fig. S1 in Supporting information). The microstructure of Bi_2S_3 exhibited a nanorod-like morphology with a length of ~200 nm and a width of ~50 nm (Figs. 1b and c). The high-resolution TEM (HRTEM) image of Bi_2S_3 shown in Fig. 1d revealed two sets of crystal lattice fringes with interplane spacing of 0.375 nm and 0.357 nm, corresponding to the (101) and (130) index planes. The morphologies of the Bi_2S_3/IG composite were shown in Figs. 1e and f, where the Bi_2S_3 nanorods were dispersed throughout the graphene skeleton structure. Interestingly, the graphene encapsulation further confined the growth of Bi_2S_3 nanorods to a length of ~100 nm and a width of ~30 nm. The interfacial boundary of Bi_2S_3 and iodine-doped graphene could be seen in the HRTEM image of the complex (Fig. 1g). The observed blur of the Bi_2S_3 lattice fringes could be linked to the overlaying of graphene sheets. Besides, the element distribution mapping results of Bi_2S_3/IG were displayed in Fig. S2 (Supporting information), demonstrating the presence of iodine.

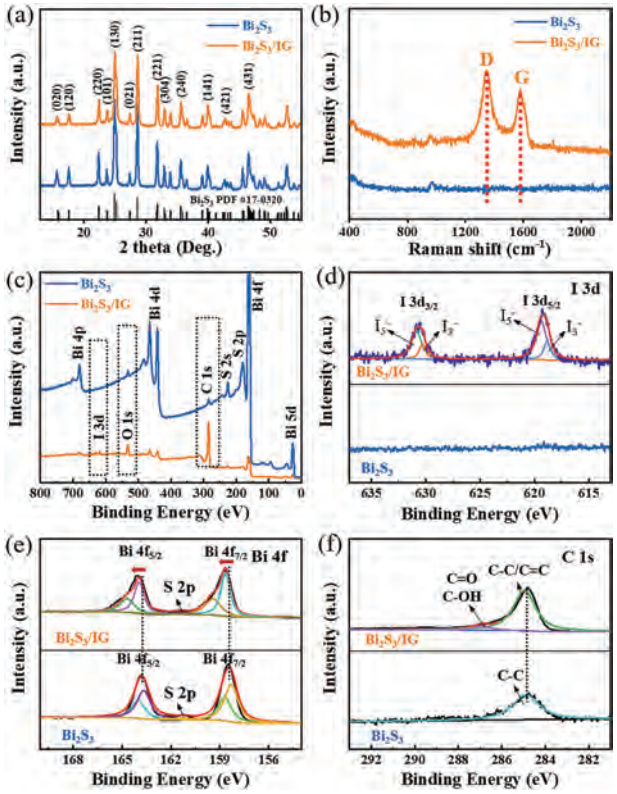

Fig. 2. Characterization of Bi_2S_3 and Bi_2S_3/IG. (a) XRD pattern of Bi_2S_3 and Bi_2S_3/IG, with the standard PDF card of orthorhombic Bi_2S_3 for identification. (b) Raman spectra of Bi_2S_3 and Bi_2S_3/IG. (c) Survey XPS spectrum of Bi_2S_3 and Bi_2S_3/IG, the dotted boxes marked the differences in peaks between the two samples. High-resolution (d) I 3d, (e) Bi 4f, and (f) C 1s XPS spectra of the Bi_2S_3 and Bi_2S_3/IG.

X-ray diffraction (XRD) pattern was employed to investigate the crystal structure of the Bi_2S_3 and Bi_2S_3/IG (Fig. 2a). The Bi_2S_3 consisted of peaks indexed to the orthorhombic crystal system referenced against PDF card (Bi_2S_3, #17–0320). The main crystal planes were marked in the spectrum. Besides, the XRD pattern of the precursor BiOI was provided in Fig. S3 (Supporting information), with major peaks indexed to the tetragonal crystal lattice structure. Fig. 2b showed the Raman spectra of Bi_2S_3/IG in reference to the Bi_2S_3, where the obvious D and G peaks of carbon confirmed the existence of graphene in the former.

X-ray photoelectron spectroscopy (XPS) further revealed the presence of iodine and the interaction between Bi_2S_3 and graphene in the composite. Fig. 2c showed the full XPS spectra of the Bi_2S_3 and Bi_2S_3/IG, where the I 3d peak appeared in the Bi_2S_3/IG composite, while the peaks of O 1s and C 1s were strengthened significantly compared with the pure Bi_2S_3. The rise in binding energy for carbon and oxygen within the composite further confirmed the existence of graphene with oxygen-containing groups. Moreover, the emergence of iodine peaks demonstrated that iodine doping had been successful. Since no iodine peak was seen for Bi_2S_3 and the associated XRD pattern did not alter, it was fair to infer that the iodine atoms doped predominantly inside graphene sheets. The high-resolution I 3d XPS spectrum of the Bi_2S_3/IG was displayed in Fig. 2d, where the peaks at 630.8 and 619.3 eV belonged to I_5^- $3d_{5/2}$ and I_5^- $3d_{3/2}$, and the peaks at 630.3 and 618.8 eV belonged to I_3^- $3d_{5/2}$ and I_3^- $3d_{3/2}$, respectively [37,38]. The iodine-doping in graphene could led to the formation of iodide polyanions which facilitated the improvement of electrical conductivity and chemical activity, resulting in rapid charge transfer and enhanced charge density [39]. As for the high-resolution XPS spectrum of Bi 4f (Fig. 2e), the peaks of Bi_2S_3/IG shifted towards

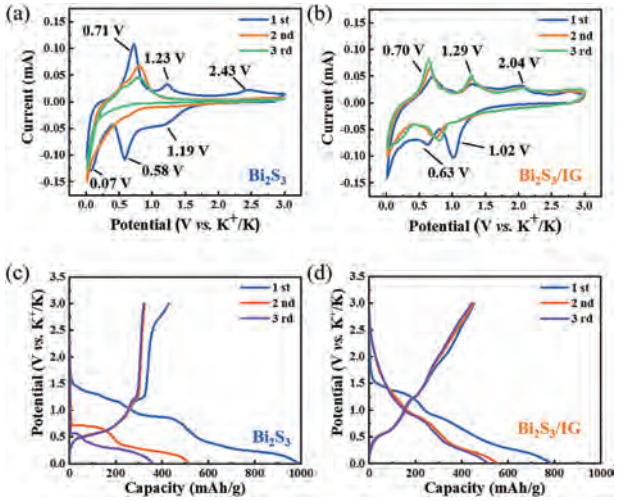

Fig. 3. Electrochemical behaviors of the Bi_2S_3 and Bi_2S_3/IG in 5 mol/L KFSI/DME electrolyte. CV curves of (a) Bi_2S_3 and (b) Bi_2S_3/IG at a scan rate of 0.1 mV/s. Initial three galvanostatic discharge/charge curves of (c) Bi_2S_3 and (d) Bi_2S_3/IG at a current density of 50 mA/g.

the high binding energy compared with that of Bi_2S_3, confirming the strong interaction between Bi_2S_3 and IG. This interfacial electron migration resulted in strong polarization and electron field at the interface, which was conducive to higher electrochemical activity [34]. The C 1s spectra (Fig. 2f) showed enhanced peaks of C=O/C-OH bonds, which belonged to the residual surface groups of graphene.

Half-batteries were assembled to examine the potassium storage behavior of the Bi_2S_3/IG composite. Three electrolytes (*i.e.*, 1 mol/L KFSI in EC/DEC, 1 mol/L KFSI in DME, and 5 mol/L KFSI in DME) were used for Bi_2S_3 and Bi_2S_3/IG electrodes to optimum the potassium storage performance. The corresponding cyclic voltammograms (CV) and galvanostatic charge/discharge curves of the Bi_2S_3 and Bi_2S_3/IG in these three electrolytes were shown in Fig. 3, Figs. S3 and S4 (Supporting information). As seen, the Bi_2S_3 electrode had a poor CV reversibility regardless of the nature of electrolyte. In contrast, the reversibility was significantly improved post iodine doping and graphene encapsulation as in Bi_2S_3/IG. The discharge-charge curves of the Bi_2S_3 further exhibited low initial Coulombic efficiencies of 40.1%, 47.8% and 43.6% in the ester and ether-based electrolytes (Fig. S4b and S5b in Supporting information, Fig. 3c), respectively. In the case of the Bi_2S_3/IG electrode, the initial Coulombic efficiency in ester electrolytes (Fig. S4d, 54.5%) was also a little lower than those in the ether electrolytes (Fig. S5d in Supporting information, 57.6% and Fig. 3d, 57.8%). Thus ether-based electrolytes might be preferable to Bi_2S_3-based electrodes. Figs. 3a and b showed the CV curves of the Bi_2S_3 and Bi_2S_3/IG electrodes in a potential range from 0.01 to 3.0 V (*vs.* K^+/K) at a scan rate of 0.1 mV/s with 5 mol/L KFSI in DME as electrolyte. As seen, three peaks located at 1.19, 0.58 and 0.07 V were found in the initial cathodic scan. The peak at 1.19 V could be ascribed to the formation of a solid electrolyte interphase (SEI) film and the conversion of Bi_2S_3 to Bi and K_2S, while the other two peaks reflected the alloying process between Bi and K^+, resulting in numerous K_xBi molecules [40]. The first anodic scan also showed three peaks near 0.71, 1.23 and 2.43 V, respectively. The peaks at 0.71 and 1.23 V represented the dealloying reaction of K_xBi to Bi, whereas the peak at 2.43 V signified the weak conversion reaction from Bi and K_2S to Bi_2S_3. Interestingly, these anodic peaks of Bi_2S_3 later weakened or disappeared in the subsequent cycles, which could be attributed to the low reversibility of conversion reactions and the structural collapse of the electrode. Although no new peaks were identified in the case of Bi_2S_3/IG, the reversibility of CV curves readily improved, suggesting a kinetic facilitation with iodine-doped graphene encapsulation. The cathodic peak at ~1.02 V later weakened in the second and third cycles, indicating the formation of SEI layer and the weak process of the conversion reaction. The peaks at ~0.63 V shifted to higher potential in the subsequent cycles, which could be attributed to the structural refinement of the electrode materials. Figs. 3c and d showed the galvanostatic charge/discharge curves of Bi_2S_3 and Bi_2S_3/IG electrodes. The potential plateaus in discharge/charge curves were nearly identical to those seen in CV curves. Compared with the Bi_2S_3, enhanced initial coulombic efficiency with inhibited capacity attenuation was realized in Bi_2S_3/IG.

To further investigate the influence of electrolytes on potassium storage performance, cycling performances in the above three electrolytes were conducted for the Bi_2S_3 electrode at 200 mA/g, as shown in Fig. S6 (Supporting information). The Bi_2S_3 electrode had the highest capacity and the best cycle stability with the 5 mol/L KFSI in DME electrolyte. The rate performance of Bi_2S_3 electrode was tested at different current densities, where the Bi_2S_3 with 5 mol/L KFSI in DME exhibited the highest capacity retention at enhanced current density. The improved chemical characteristics of Bi_2S_3 in ether electrolytes might be derived from its ability to produce a more stable SEI layer on the Bi_2S_3 surface and prompt kinetic process of potassium ion storage [41]. Fig. S7 (Supporting information) showed the electrochemical performances of Bi_2S_3/IG electrodes in the above three electrolytes with relatively improved performance realized in 5 mol/L KFSI in DME. According to the HOMO (highest occupied molecular orbital) and LUMO (lowest unoccupied molecular orbital) energy levels of KFSI, KPF_6, DME, EC and DEC, the KFSI salt owns more reactive feature, while the DME solvent owns a more inactive characteristic [42–45]. Thus, when KFSI/DME electrolyte is selected, KFSI is preferred to form a robust inorganic SEI layer on the electrode surface rather than solvent decomposition, which can inhibit the growth of potassium dendrites [46,47]. Meanwhile, concentrated KFSI electrolyte can enhance the stability of the solvent [47,48]. These characteristics enabled Bi_2S_3/IG to perform higher Coulombic efficiency and better cyclic stability with the electrolyte of 5 mol/L KFSI in DME. As a result, 5 mol/L KFSI in DME electrolyte was chosen as the optimum electrolyte for comparing the potassium storage performance of the Bi_2S_3 and Bi_2S_3/IG electrode.

The cycling performances of Bi_2S_3 and Bi_2S_3/IG electrodes at 100 mA/g for 200 cycles were shown in Fig. 4a, which were pre-activated at a low current density of 50 mA/g for the initial three cycles before the long-term cycle testing. The Bi_2S_3 electrode showed an initial reversible capacity of 242.1 mAh/g with a maintained capacity of only 94.9 mAh/g after 200 cycles. In contrast, the Bi_2S_3/IG composite revealed an initial reversible capacity of 413.6 mAh/g with a maintained capacity of 256.9 mAh/g after 200 cycles. The rate performances of Bi_2S_3 and Bi_2S_3/IG electrodes were evaluated by varying the current density from 50 mA/g to 2000 mA/g (Fig. 4b). Here, the Bi_2S_3/IG electrode delivered reversible capacities of 453.5, 373.5, 304.8, 241.0, 169.9 and 78.2 mAh/g at different current densities of 0.05, 0.1, 0.2, 0.5, 1 and 2 A/g, respectively, much higher than those of the Bi_2S_3 electrode, which lost its work ability at 500 mA/g. The results indicated that the addition of iodine-doped graphene could effectively increase the potassium storage performances of the Bi_2S_3. Meanwhile, Fig. S8 (Supporting information) provided the rate capabilities of pure graphene electrode with 5 mol/L KFSI in DME as electrolyte. Fig. 4c showed the electrochemical impedance spectroscopy (EIS) of Bi_2S_3 and Bi_2S_3/IG electrodes with the 5 mol/L KFSI in DME electrolyte. The charge transfer resistance (R_{ct}) of Bi_2S_3 reduced dramatically when the iodine-doped graphene was introduced, as evident by the lower semicircle diameter of the Bi_2S_3/IG electrode, which was

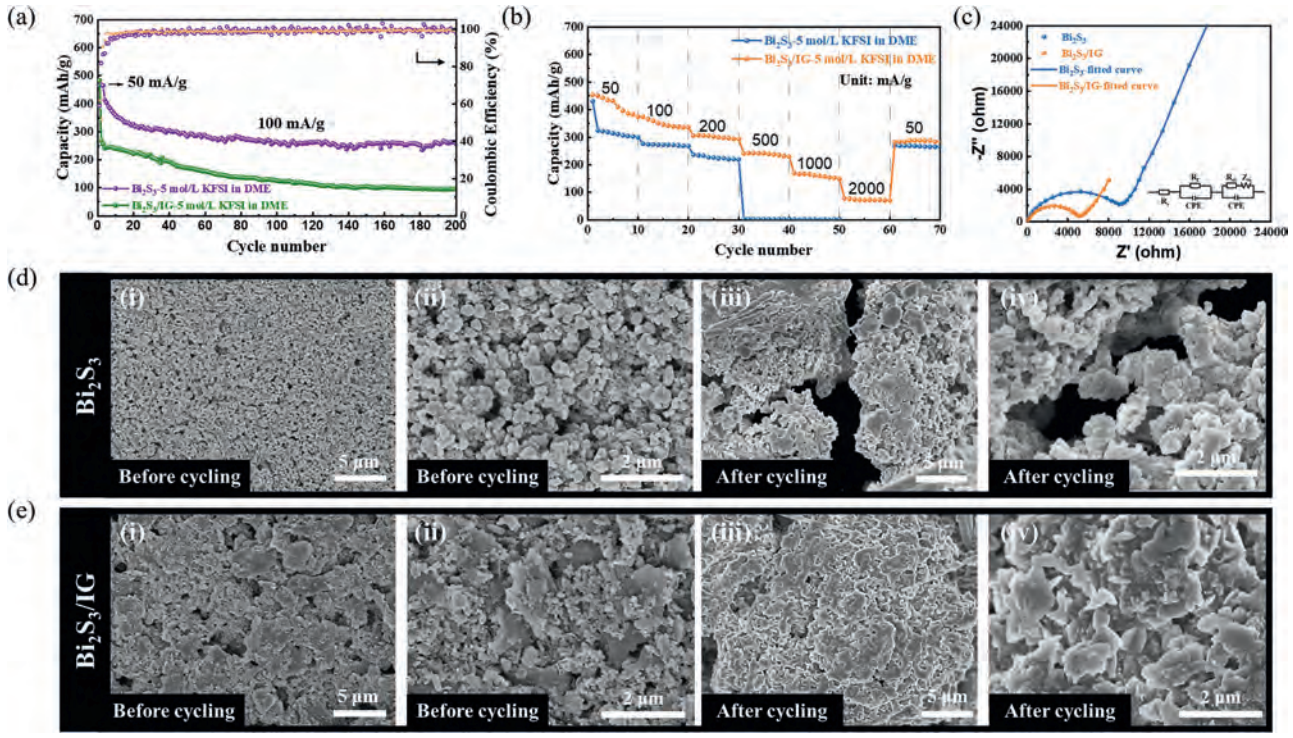

Fig. 4. Electrochemical properties of Bi_2S_3 and Bi_2S_3/IG as electrode materials. (a) Cycle performance of Bi_2S_3 and Bi_2S_3/IG at 100 mA/g in 5 mol/L KFSI in DME electrolyte. (b) Rate capabilities of Bi_2S_3 and Bi_2S_3/IG from 50 mA/g to 2 A/g in 5 mol/L KFSI in DME electrolyte. (c) Nyquist plots of the Bi_2S_3 and Bi_2S_3/IG with corresponding fitting circuit. (d) The morphologies of Bi_2S_3 electrode (i, ii) before and (iii, iv) after cycling. (e) The morphologies of Bi_2S_3/IG electrode (i, ii) before and (iii, iv) after cycling.

responsible for the superior electron transfer efficiency and good rate performance of the Bi_2S_3/IG composite. The Nyquist plots of Bi_2S_3 and Bi_2S_3/IG with their fitting curves in 1 mol/L KFSI in EC/DEC and 1 mol/L KFSI in DME were provided in Fig. S9 (Supporting information), which showed similar rule. Figs. 4d and e showed the morphologies of the Bi_2S_3 and Bi_2S_3/IG electrodes before and after cycling, respectively. The surface of both electrodes had good flatness before cycling. However, obvious cracks were observed for the Bi_2S_3 electrode post cycles at 100 mA/g, explaining its fast-declining capacity. By contrast, after adding the iodine-doped graphene, the structural stability of the Bi_2S_3/IG electrode was obviously improved. No obvious crack can be observed on the surface of Bi_2S_3/IG electrode after cycling, which was responsible for the better cycling stability.

In conclusion, we proposed a Bi_2S_3/IG composite as an efficient anode for PIBs. Compared with the pure Bi_2S_3, the interaction between Bi_2S_3 and iodine-doped graphene realized a more stable structure with improved electron transfer rate, enhancing the overall potassium storage performances of the Bi_2S_3-based materials in terms of capacity, cycle performance, and rate performance. The electrochemical performances of Bi_2S_3 and Bi_2S_3/IG electrodes were also investigated in three different electrolytes, with 5 mol/L KFSI in DME as the best choice. The representative Bi_2S_3/IG composite achieved a high specific capacity of 453.5 mAh/g at a current density of 50 mA/g with good cycling performance at 100 mA/g. The constructed Bi_2S_3/IG composite and the proposed iodine doping graphene approach are expected to improve the performance of potassium ion batteries and related electrochemical applications.

Declaration of competing interest

The authors declare that they have no known competing financial interests or personal relationships that could have appeared to influence the work reported in this paper.

Acknowledgments

This work was financially supported by the National Natural Science Foundation of China (No. 52072021).

Supplementary materials

Supplementary material associated with this article can be found, in the online version, at doi:10.1016/j.cclet.2021.10.035.

References

[1] Y.C. Liu, B. Huang, Y.J. Shao, et al., Prog. Chem. 31 (2019) 1329–1340.
[2] W.L. Zhang, J. Yin, W.X. Wang, Z. Bayhan, H.N. Alshareef, Nano Energy 83 (2021) 105792.
[3] N. Sun, Q. Zhu, B. Anasori, et al., Adv. Funct. Mater. 29 (2019) 1906282.
[4] P. Zhang, R.A. Soomro, Z. Guan, N. Sun, B. Xu, Energy Storage Mater. 29 (2020) 163–171.
[5] Z. Jian, W. Luo, X. Ji, J. Am. Chem. Soc. 137 (2015) 11566–11569.
[6] B. Cao, H. Liu, P. Zhang, et al., Adv. Funct. Mater. 31 (2021) 2102126.
[7] Z.L. J.ian, S. Hwang, Z.F. Li, et al., Adv. Funct. Mater. 27 (2017) 1700324.
[8] W. Hong, Y. Zhang, L. Yang, et al., Nano Energy 65 (2019) 104038.
[9] X. Wu, Y. Chen, Z. Xing, et al., Adv. Energy Mater. 9 (2019) 1900343.
[10] Y. Xu, J. Zhang, D. Li, Chem. Asian J. 15 (2020) 1648–1659.
[11] Y. Zhang, J. Lou, Y. Shuai, et al., Mater. Lett. 242 (2019) 5–8.
[12] W. Li, Z. Bi, W. Zhang, et al., J. Mater. Chem. A 9 (2021) 8221–8247.
[13] I. Sultana, M.M. Rahman, S. Mateti, et al., Nanoscale 9 (2017) 3646–3654.
[14] J. Chen, D.H.C. Chua, P.S. Lee, Small Methods 4 (2020) 1900648.
[15] Q. Pan, Z. Tong, Y. Su, S. Qin, Y. Tang, Adv. Funct. Mater. (2021) 2103912.
[16] S. Geng, T. Zhou, M. Jia, et al., Energy Environ. Sci. 14 (2021) 3184–3193.
[17] S. Ghosh, Z.M. Qi, H.Y. Wang, S.K. Martha, V.G. Pol, Electrochim. Acta 383 (2021) 138339.
[18] X.D. Ren, Q. Zhao, W.D. McCulloch, Y.Y. Wu, Nano Res. 10 (2017) 1313–1321.
[19] Z. Chen, D.G. Yin, M. Zhang, Small 14 (2018) 1703818.
[20] J.H. Choi, G.D. Park, Y.C. Kang, Chem. Eng. J. 408 (2021) 127278.
[21] Y.F. Xu, J.L. Sun, Y.N. He, et al., Sci. China Chem. 64 (2021) 1401–1409.
[22] Q.Q. Yao, J.S. Zhang, X.L. Shi, et al., Electrochim. Acta 307 (2019) 118–128.
[23] Y. Zhao, J.J. Zhu, S.J.H. Ong, et al., Adv. Energy Mater. 8 (2018) 1802565.
[24] Z.C. Zhao, Z.Q. Hu, R.S. Jiao, et al., Energy Storage Mater. 22 (2019) 228–234.
[25] X.X. Jia, E.J. Zhang, X.Z. Yu, B.A. Lu, Energy Technol. 8 (2020) 1900987.
[26] C. Nithya, G. Thiyagaraj, Sustain. Energy Fuels 4 (2020) 3574–3587.
[27] T.H. Wang, D.Y. Shen, H. Liu, et al., ACS Appl. Mater. Interfaces 12 (2020) 57907–57915.

[28] V. Lakshmi, A.A. Mikhaylov, A.G. Medvedev, et al., J. Mater. Chem. A 8 (2020) 11424–11434.
[29] Y. Zhang, P. Wang, Y. Yin, et al., Chem. Eng. J. 356 (2018) 1042–1051.
[30] Q.K. Peng, S.P. Zhang, H. Yang, et al., ACS Nano 14 (2020) 6024–6033.
[31] W.D. Li, D.Z. Wang, Z.J. Gong, et al., ACS Nano 14 (2020) 16046–16056.
[32] W.W. Chai, F. Yang, W.H. Yin, et al., Dalton Trans. 48 (2019) 1906–1914.
[33] W.P. Sun, X.H. Rui, D. Zhang, et al., J. Power Sources 309 (2016) 135–140.
[34] Y.H. Liu, M.L. Li, Y.Y. Zheng, et al., Nanoscale 12 (2020) 24394–24402.
[35] Y. Zhang, L. Fan, P. Wang, et al., Nanoscale 9 (2017) 17694–17698.
[36] C. Wang, J. Lu, H. Tong, et al., Nano Res. 14 (2021) 3545–3551.
[37] Z. Yao, H. Nie, Z. Yang, et al., Chem. Commun. 48 (2012) 1027–1029.
[38] J. Yang, J. Zhang, X. Li, et al., Nano Energy 53 (2018) 916–925.
[39] Z. Xiao, Z. Yang, L. Zhang, H. Pan, R. Wang, ACS Nano 11 (2017) 8488–8498.
[40] C. Shen, G. Song, X. Zhu, et al., Nano Energy 78 (2020) 105294.
[41] K. Li, J. Zhang, D. Lin, et al., Nat. Commun. 10 (2019) 725.
[42] L. Fan, S. Chen, R. Ma, et al., Small 14 (2018) 1801806.
[43] L. Zhou, Z. Cao, J. Zhang, et al., Adv. Mater. 33 (2021) 2005993.
[44] J. Zhang, Z. Cao, L. Zhou, et al., ACS Energy Lett. 5 (2020) 3124–3131.
[45] X. Min, J. Xiao, M. Fang, et al., Energy Environ. Sci. 14 (2021) 2186–2243.
[46] J. Wang, B. Wang, B. Lu, Adv. Energy Mater. 10 (2020) 2000884.
[47] L. Fan, R. Ma, Q. Zhang, X. Jia, B. Lu, Angew. Chem. Int. Ed. 58 (2019) 10500–10505.
[48] K.T. Chen, H.Y. Tuan, ACS Nano 14 (2020) 11648–11661.